



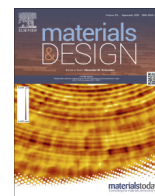
Design and characterization of a cobalt-free stainless maraging steel for laser-based powder bed fusion

Downloaded from: <https://research.chalmers.se>, 2024-04-23 18:39 UTC

Citation for the original published paper (version of record):

Riabov, D., Frisk, K., Thuvander, M. et al (2022). Design and characterization of a cobalt-free stainless maraging steel for laser-based powder bed fusion. *Materials and Design*, 223. <http://dx.doi.org/10.1016/j.matdes.2022.111180>

N.B. When citing this work, cite the original published paper.



Design and characterization of a cobalt-free stainless maraging steel for laser-based powder bed fusion

D. Riabov^{a,*}, K. Frisk^a, M. Thuvander^c, E. Hryha^a, S. Bengtsson^b

^aIndustrial Materials and Science, Chalmers University of Technology, Gothenburg 412 96, Sweden

^bHöganäs AB, Höganäs 263 39, Sweden

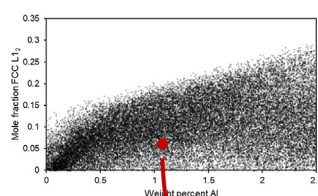
^cDepartment of Physics, Chalmers University of Technology, Gothenburg 412 96, Sweden

HIGHLIGHTS

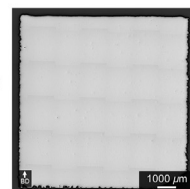
- A Co-free stainless maraging steel for laser-based powder bed fusion was successfully designed using a computation alloy design approach.
- The material showed excellent printability with a porosity of <0.05% and a fully martensitic microstructure in the as-built condition.
- Aging at 500 °C was performed directly after printing, where an increase from 310 HV5 to 519 HV5 was noted.
- Ni, Al, Ti, Nb, Mn and Si were found to readily form precipitates – believed to be γ' after 3 h.
- The precipitates were also found to be resistant to coarsening, retaining high hardness even after 90 h at 500 °C.

GRAPHICAL ABSTRACT

Screening from 40 000 compositions



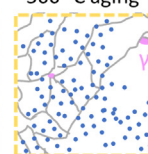
Excellent printability



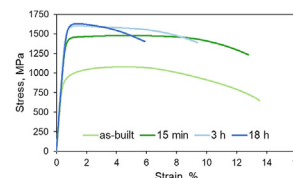
As-built



500 °C aging



Ni, Al, Ti, Nb, Mn, Si precipitates



Rapid precipitation response

ARTICLE INFO

Article history:

Received 10 May 2022

Revised 7 September 2022

Accepted 19 September 2022

Available online 20 September 2022

Keywords:

Additive
LB-PBF
Maraging
APT
Precipitates
Alloy design

ABSTRACT

This study presents a new Co-free stainless maraging variant for laser-based powder bed fusion developed using a computational alloy design approach. The goal was to develop an easily printable material with similar performance to 18Ni-300. After screening numerous compositions, Fe-13.2Cr-9.1Ni-1.1Al-0.6Mo-0.5Nb-0.23Ti-0.5Mn-0.5Si (wt.%) was selected. This composition showed excellent printability with low porosity levels. The precipitation strengthening response was evaluated by aging at 500 °C for 15 min, 3 h and 18 h, measuring hardness, tensile strength, and by characterization using atom probe tomography. After 15 min of aging, 90% of the maximum hardness was reached, thanks to formation of (Ni, Al, Nb, Ti, Mn, Si) clusters with a density of $1.5 \times 10^{24} \text{ m}^{-3}$. Between 15 min and 3 h, distinct precipitates formed with a radius of $\sim 1.4 \text{ nm}$. The precipitates underwent a splitting phenomenon after 18 h, forming several unique Ni-rich precipitates including $\text{Ni}_{16}\text{Si}_7(\text{Ti, Nb})_6$ and $\text{Ni}_3(\text{Al, Ti, Nb, Si})$. The splitting can be a reason for the slow coarsening rate, as the average precipitate radius after 18 h was only 2 nm. Simulations of the precipitation sequence using PRISMA indicated very rapid and dense precipitation of $\text{L}_{12}\text{-Ni}_3\text{X}$ precipitates with a slow coarsening rate, in agreement with experimental observations.

© 2022 The Authors. Published by Elsevier Ltd. This is an open access article under the CC BY license (<http://creativecommons.org/licenses/by/4.0/>).

* Corresponding author: Department of Industrial and Materials Science, Chalmers University of Technology, Rännvägen, 2A, SE-412 96 Gothenburg, Sweden.
E-mail address: riabov@chalmers.se (D. Riabov).

1. Introduction

High-performance steels, such as the maraging steels, are a class of materials that combine high strength and toughness. Therefore, they are often considered paramount for lightweight designs and future reduction in emissions [1]. These properties are enabled by a combination of a ductile martensitic matrix and intermetallic precipitates that form within the matrix. Due to the combination of mentioned properties, this material group has been shown to have excellent printability in additive manufacturing (AM), specifically laser-based powder bed fusion (LB-PBF) [2].

Excellent printability can be a challenge to achieve, however, several alloy specific properties can greatly improve it. These include but are not limited to: sufficient ductility of the matrix phase – needed to accommodate strains that are induced during the repeated solidification; that elemental segregation is kept to a minimum, avoiding the formation of brittle or low-melting phases, which could cause crack formation; and finally that the alloy has a narrow solidification range – reducing the risk of hot tearing [3].

Laser-based powder bed fusion is an AM technology where metal powder is iteratively melted using a high-powered laser to produce a component [4–6]. Due to the small size of the laser spot and high laser scanning velocities, the resulting heating and cooling rates are very high, up to 10^7 K/s [7–9]. The rapid solidification creates very fine microstructures with specific features and, when alloying is balanced, a supersaturated matrix [10]. Therefore, when selecting material compositions for AM there is a benefit in adjusting the composition to the process as the microstructures resulting from LB-PBF are quite different to those obtained in conventionally processed materials.

A common maraging steel for AM, 18Ni-300, contains high Co-contents (~9 wt%). Because of the toxicity of Co and problematic mining operations [11–14] there is a need to expand the number of alloys without this alloying element. Hence, a Co-free maraging-type steel powder was designed aiming for good printability, corrosion resistance and good temperature resistance. To obtain the desired composition a CALPHAD-based (CALculation of PHase Diagrams) computational alloy development procedure was used. Calculations of equilibrium phase compositions were combined with kinetic modeling of the phase transformations, and a procedure of scanning over wide compositional ranges was used. The Thermo-Calc software and databases, TCFE9 and TCNi8, [15] were used for the calculations.

The design of the material was guided by previous work on 18Ni-300 [2,16–21]. The as-printed material has a fine cellular/dendritic microstructure that is martensitic with 6–11% retained austenite. The amount of retained austenite depends on the printing conditions. High amounts of retained austenite are generally considered detrimental to the peak hardness and strength [19] as precipitation does not take place in austenite, hence, requiring additional heat treatments prior to aging. However, the critical amount can vary depending on the application – where some retained austenite can be beneficial to the overall ductility of the alloy. The alloy 18Ni-300 is relatively soft with high ductility in the as-printed condition, hence the good printability, and is strengthened by aging in the temperature range 490–530 °C. For AM processed 18Ni-300 there are two possible heat treatment routes: conventional heat treatments (solution annealing and aging) or directly aging the as-printed condition. Typical hardness values in the as-printed condition are 350–400 HV and after aging 550–650 HV [2,20]. The yield stress at peak hardness is around 2 GPa with an elongation to fracture of 1.5–5% [2].

A major drawback with the 18Ni-300 grade is the poor corrosion resistance, which can be improved by Cr additions. However, this necessitates further modification of the composition. Stainless maraging steels have existed for some time and most common

variants, such as 13-8Mo, typically rely on Ni and Al as the primary precipitation forming elements. The formed precipitate is NiAl with a fully coherent B2 superlattice structure, with a cube-on-cube orientation relationship with the matrix [22–24]. The size of the precipitates is only around 10 nm even after prolonged aging, with high number densities of $\sim 10^{24}$ m³ [22,23,25]. The composition of the precipitates was found to deviate from perfect stoichiometry; where the fraction of Al increased from around 10at% after aging for 0.5 h at 450 °C to nearly 40at% after 500 h [23]. Other variants, such as Custom 465® and Nanoflex®, rely instead on Ni and Ti as the precipitate forming elements [26,27]. Here, the dominant precipitate is η -Ni₃Ti, with a hexagonal (DO₂₄) structure and an orientational relationship to the martensitic matrix according to: (011)_M//(0001) _{η} ; [111]_M//[1120] _{η} [28,29]. In Nanoflex®, another dominant precipitate is γ' -Ni₃(Ti, Al, Si) with a L1₂ structure [26]. η -Ni₃Ti forms as rods, typically between 10 and 20 nm in length and a few nm in diameter, while γ' forms as spheres [27,30,31]. It was also found that Al can readily substitute Ti in η -Ni₃Ti, hence the precipitates can contain both Al and Ti [32]. Apart from the mentioned precipitates, formation of G-phase (Ni₁₆Si₇Ti₆) [26], a Mo-rich quasicrystalline phase called R' and Cr rich α' have also been reported in stainless maraging steels after prolonged aging times [33,34].

Additive manufacturing of maraging steels have mostly been focused on the 18Ni-300 grade, with few studies on stainless variants. Jägle et al. [19] compared the microstructures of conventionally produced, laser metal deposited and LB-PBF processed 18Ni-300 and reported that precipitate kinetics, size and composition remained similar despite different manufacturing routes. The printed stainless variants have mostly been 13-8Mo derivatives, including CX® from EOS and Corrax® from Uddeholm. The results indicated good printability with minimal retained austenite, forming B2 structured NiAl precipitates upon aging [35–39]. However, characterization was performed mostly by transmission electron microscopy (TEM), with an exception in the study of Corrax® by Krakhmalev et al. where atom probe tomography (APT) was utilized and precipitates with a 1:1 ratio of Ni and Al were found. Hence, detailed precipitate descriptions were, for the most part, not given.

The degree of strengthening that can be gained from precipitates will depend on numerous factors, such as the size, volume fraction and strength of the precipitate. Typically, hard particles (where the strength of the particle supersedes the line tension of the dislocation) will cause dislocations to loop around them. Soft particles are instead sheared by the dislocations, creating an anti-phase boundary that will provide a strengthening effect [40–43]. Niu et al. reported that a maraging steel with mainly η -Ni₃Ti precipitates will undergo both modes of interaction depending on aging time [30]. Initially, small Ni, Ti, Mo clusters are cut while during the later stages the precipitates are by-passed through the looping (Orowan) mechanism. Similarly, Schnitzer et al. [44] modelled the strengthening response of 13-8Mo (strengthened primarily by B2-NiAl precipitates) and found that none of the classical precipitation models accurately described the aging response. Instead, as the findings of Niu et al., the distribution of precipitate sizes gives rise to a mixed dislocation interaction, where the smallest particles are sheared, and the larger particles are by-passed by looping.

2. Materials and methods

2.1. Computational alloy design

A computational procedure was used for the alloy design, and the computations were performed using CALPHAD-type predic-

tions of the phase equilibria, and simulation of the precipitation evolution. The Thermo-Calc software [15] was used to perform the calculations of the phase equilibria. The high temperature phase equilibria were calculated using the TCFE9 database, and the low temperature equilibria involving the precipitating phases were calculated using the TCNi8 database. The high temperature equilibria involved a calculation of the Cr content of austenite including the martensite forming temperature, and the amount of retained austenite. The phase equilibria at 450 to 500 °C were calculated to determine the type and amount of possible precipitates. The calculations were performed for 40 000 possible alloy compositions within a selected composition range. Analysis of the generated dataset was used to select an optimal composition.

2.2. Experimental procedure

Powder was vacuum induction melted and argon gas atomized by Höganäs AB and provided in the 15–45 µm sieve fraction. Cubes of size $10 \times 10 \times 10 \text{ mm}^3$ were printed using LB-PBF for evaluation of the material properties in an EOS M290 (Electro Optical Systems, GmbH) machine using the standard parameters for 18Ni-300 (MS1_040_PerformanceM291 2.0) using a layer thickness of 40 µm. An overview of the LB-PBF process was given by Sun et al. [45]. The scan vector was rotated 67° after each layer exposure and a stripe scanning strategy was employed. Argon was used as the protective atmosphere and the oxygen partial pressure was kept below 0.1% throughout the build. No build plate pre-heating was used.

The cubes were directly aged after printing. The aging was done at 500 °C for 15 min, 30 min, 1 h, 3 h, 9 h, 18 h, and 90 h. The short times, 15 and 30 min were used to investigate the initial clustering. The use of 1, 3 and 9 h were because these times are used in conventional aging treatments of similar maraging steels. Finally, 18 and 90 h were used to evaluate the long-term thermal stability of the precipitates. The procedure was performed in a lab scale tube furnace with argon as a protective gas to minimize oxidation. All samples were water quenched after the aging process. Subsequent microstructural and mechanical evaluations focused on the 15 min, 3 h, and 18 h states.

Sectioning and subsequent mounting of the cubes in conductive resin were done to evaluate the printed density, resulting microstructure and the aging response. The mounted specimens were prepared according to the following procedure: initial plane grinding using 220 grit SiC paper, followed by fine grinding using 9 µm diamond suspension and polishing using 3 µm followed by 1 µm diamond suspension. As a final polishing step, 0.05 µm colloidal silica was used.

Light optical microscopy (LOM) was used to evaluate the printed density on as-built cubes, a Zeiss Axioscope 7 was used in this process. Samples were etched using Kalling's solution to evaluate the printed microstructures, which were documented using LOM. Grain morphology, orientation and phase constituents were measured using electron backscatter diffraction (EBSD). For the EBSD acquisitions the field-emission scanning electron microscope (SEM) Hitachi SU6600 equipped with an Oxford Symmetry 1 EBSD detector with a CMOS sensor was used. The maps were acquired using a voltage of 20 kV with a step size of 0.08 µm and the data was analyzed using the MTEX toolbox [46]. The fracture surfaces were analyzed using a LEO Gemini 1550 field-emission SEM operating at 2 kV. Detailed microstructural characterization was performed with TEM where an FEI Tecnai T20 operating at 200 kV was utilized. Thin foils were prepared from sections parallel to the building direction by mechanically thinning samples down to around 100 µm followed by electrolytic twin-jet polishing at a voltage of 16 V until perforation using a 10% perchloric solution that was cooled to -30 °C.

For preparing samples for APT, rods of approximate dimensions $0.3 \times 0.3 \times 15 \text{ mm}^3$ were made by coarse cutting, grinding and final cutting using a low-speed diamond saw. Ultra-sharp samples were then prepared using a two-stage electropolishing procedure. In the first stage, a neck was created by polishing in a layer of a strong electrolyte (10% perchloric acid in glycerol (20%) and methanol (70%)) floating atop a heavy inert liquid (Galden). In the second stage, the entire rod was polished in a weak electrolyte (2% perchloric acid in 2-butoxyethanol) until the part below the neck was separated at the position of the neck made in the first stage. The samples were further polished using pulsed polishing (2–10 pulses of 1–10 ms duration) in the weak electrolyte, to clean the surface. All polishing was made at around 18 V, and Pt was used as cathode.

The used atom probe was a LEAP 3000X HR (Imago Scientific Instruments), which has a detection efficiency of 37%. The analyses were made in laser pulse mode, with a laser wavelength of 532 nm at a pulse frequency of 200 kHz, laser pulse energy 0.30 nJ, sample temperature 50 K and evaporation rate 0.20%. The reconstructions were made using the voltage method, with an image compression factor of 1.65, a field factor of 3.0–4.0 and an evaporation field of 25 V/nm. Iso-concentration surfaces (isosurfaces) were obtained using a cubic voxel size of 1.0 nm^3 and with delocalization of $3 \times 3 \times 1.5 \text{ nm}^3$. The statistical tools radial distribution function (RDF) [47] and maximum separation method (MSM) [48] were used to study co-precipitation tendencies and early clustering, respectively.

The use of laser pulsing, instead of voltage pulsing, has both advantages and disadvantages. The analyses generally gets longer (larger analysis depth) and the mass spectrum overlap between $^{93}\text{Nb}^{3+}$ and $^{62}\text{Ni}^{2+}$ is avoided (as Nb evaporates as Nb^{2+}). However, the use of laser pulsing means that Al will be evaporated as both Al^{2+} and Al^+ , the latter overlapping at 27 Da with minor isotopes of Fe^{2+} and Cr^{2+} . The distribution of Al^{2+} and Al^+ was not homogeneous, so the Al signal (13.5 Da) was clearer in some regions than in others (depending on uneven laser heating). Furthermore, Si was affected by surface diffusion, resulting in a partly incorrect distribution. This is seen as Si-rich streaks along the analysis axis.

Tensile tests were conducted at room temperature using an Instron 4505-5500R machine, with strain-rate control at a rate of 0.001 s^{-1} . A miniature specimen geometry as described in [49] was used. Samples were spark machined from a horizontally oriented rectangular printed geometry. Each condition was repeated twice. Hardness was measured on polished cross-sections using a Vickers hardness indenter, with a load of 5 kgf. For this purpose, a Struers DuraScan-70 G5 was used.

3. Results

3.1. Computational alloy design

The metal powder composition was designed to obtain a martensitic matrix in the as-printed state with a maximum of 15% retained austenite. The resistance to corrosion was optimized using the pitting resistance equivalent number ($\text{PREN} = \% \text{Cr} + 3.3 \times \% \text{Mo} + 16 \times \% \text{N}$) [50] with a goal of 12 or higher. Precipitation hardening was designed for aging at 450 to 500 °C with the goal of achieving similar precipitation hardening as in 18Ni-300. Further, a target was to have an alloy with a good temperature resistance in the printed and hardened state. To achieve this goal precipitation hardening phases that show slow coarsening rates were selected.

A selection of possible composition ranges was made based on a general knowledge of the alloy systems, and the following ranges were selected; 0–3% Al, 10–25% Cr, 0–2% Nb, 8–25% Ni, 0–6% Mo,

0–2% Ti (wt.%). Cr, Ni and Mo are added to produce a martensitic and stainless steel. Al, Nb and Ti are added to form precipitates. To investigate the influence of composition on the phase equilibria a scan over possible composition ranges was made, where calculations of the phase equilibria were performed and saved, generating a large dataset. The data was analyzed based on the design criteria and through this procedure compositions that fulfilled the criteria were selected. From this first selection a manual procedure to check the compositions in detail by calculations followed. An example of the data analysis procedure is shown in Fig. 1, where the Al content of the screened alloys is related to the calculated equilibrium amount of the L_{12} -Ni₃X intermetallic phase at low temperatures, for which the major element in the second sublattice is Al. The equilibrium fraction is a measure of the maximum amount of this phase that can be expected during precipitation hardening heat treatment. Several different composition-sets of the L_{12} -Ni₃X precipitate were predicted through the calculations, and the total amount was used for the alloy selection. Each point in the diagram represents one of the calculated alloy compositions.

Following the analysis of the calculated data, a chemical composition was selected, listed in Table 1. Based on the calculations this alloy is expected to be martensitic with a retained austenite

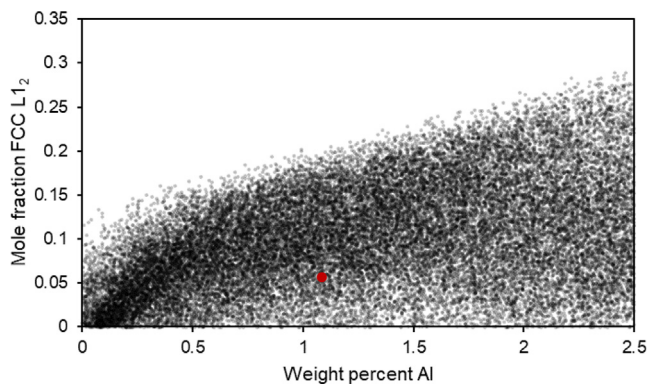


Fig. 1. The screened compositions during the alloy design process. Each dot in the figure represents one alloy composition; shown as a function of the Al content and its associated calculated mole fraction of L_{12} -Ni₃X. The red dot represents the selected composition. (For interpretation of the references to color in this figure legend, the reader is referred to the web version of this article.)

Table 1

Designed and measured chemical composition of the investigated alloy (Fe is balance).

	Element	Cr	Ni	Al	Mo	Nb	Ti	Mn	Si
Designed	wt%	13.2	9.1	1.1	0.6	0.5	0.23	0.5	0.5
Designed	at%	13.9	8.5	2.2	0.3	0.3	0.25	0.5	1
Measured	wt%	13.1	8.9	0.9	0.6	0.5	0.3	0.3	0.3
Measured	at%	13.9	8.4	1.8	0.3	0.3	0.3	0.3	0.6

Table 2

The calculated composition of the L_{12} -Ni₃X precipitates that can form during aging at 500 °C. The content of Mo is negligible.

	Ni	Al	Nb	Ti	Fe	Mn	Si	Cr
at%	72	15.2	5	4.5	1.8	1.1	0.35	0.1

Table 3

Hardness values of the investigated material, in the as-built condition and aged for various times at 500 °C.

Condition	As-built	15 min	30 min	1 h	3 h	9 h	18 h	90 h
HV 5	310 ± 3	472 ± 2	495 ± 3	506 ± 6	513 ± 4	514 ± 3	519 ± 6	501 ± 1

content of a maximum of 11%, and a maximum amount of precipitates on aging of 5.4 mol%. The precipitates that are expected to form are of the L_{12} -Ni₃X type, with the predicted composition listed in Table 2 below. The alloy has a calculated PREN number of 15.1 and is not expected to form detrimental intermetallic phases during LB-PBF processing. The selected alloy composition is optimized based on a combination of criteria. Analysis based on a single criterion will provide a large number of possible alloys, but when the criteria are considered in combination, the selected alloy is unique. If a higher amount of retained austenite, a lower PREN number, or a smaller amount of precipitates is targeted, other compositions may be selected.

3.2. Mechanical testing

The full aging response is presented below in Table 3. After heat treating at 500 °C for 15 min the hardness increased from 310 HV to 472 HV, suggesting that the precipitation was extremely rapid at this temperature. After 30 min the hardness increased to 495 HV and further aging led to only a marginal increase, reaching peak hardness of 519 HV after 18 h. After 90 h of aging the hardness dropped slightly, to 501 HV, suggesting that the precipitates are stable even during pro-longed exposure to high temperatures. Based on the aging response the following times were selected for further investigations: 15 min, 3 h, and 18 h. 15 min represented the very early stages of cluster formation, 3 h represented a typical aging time for maraging steels, while 18 h represented the peak hardness condition.

Fig. 2 presents representative stress–strain curves of the studied material in the as-built state and several aged conditions that were also evaluated using APT. Aging for a duration of 3 h at 500 °C produced a state where ductility and strength was balanced, as compared to the state that was aged for 18 h where the ductility dropped significantly while only gaining ~20 MPa in strength. Table 4 provides a summary of the data.

Fig. 3 shows the fracture surfaces of tensile test specimens. All fracture surfaces comprised primarily of dimples, indicative of a ductile fracture. However, with increasing aging times the dimples gradually became shallower, which was reflected in the lower elongation to failure with prolonged aging. After 18 h of aging occasional cleavage facets, to the right in Fig. 3h, could be observed in addition to the dimples.

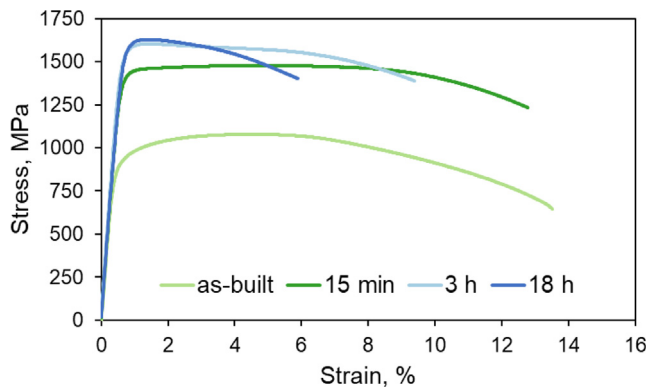


Fig. 2. Representative stress-strain curves of as-built and aged conditions.

Table 4
Summary of the mechanical properties.

Condition	Yield Strength, MPa	Ultimate Strength, MPa	Elongation, %
as-built	815 ± 50	970 ± 71	13.9 ± 0.3
15 min	1408 ± 12	1478 ± 0.1	13.4 ± 1.0
3 h	1561 ± 1.5	1604 ± 2.2	9.4 ± 1.1
18 h	1585 ± 1.4	1621 ± 12	5.9 ± 2.5

3.3. As-built microstructure

Fig. 4 presents polished cross sections, both parallel and perpendicular to the building direction, of as-built cubes. As can be seen, no large pores, inclusions or cracks could be found within the cross-sections. The residual porosity was found to be below 0.05%, as measured by LOM. This indicated that the investigated material printed to high densities without any major issues.

The polished cross sections were etched in order to investigate the microstructural constituents with the results presented in Fig. 5. The etching process revealed what visually appeared to be a fully martensitic microstructure. However, the typical LB-PBF melt-pool structure was not clearly delineated. Despite this, very faint melt pool borders could be seen at higher magnifications (also highlighted in Fig. 5).

EBSD maps of the as-built condition are shown in Fig. 6. Here, phase and orientation maps are shown with respect to two orientations, parallel to the building direction and perpendicular to it. In

both cases, the amount of retained austenite (imaged with salmon-color) was marginal (below 0.05%). In the map oriented parallel to the building direction a melt-pool grain morphology could be identified.

3.4. Aged state

The microstructure was analyzed again using EBSD after aging at 500 °C for a duration of 3 h, which can be seen below in Fig. 7. At this point, a few micrometer-sized grains were indexed as austenite hence indicating some austenite reversion. However, the total volume fraction of austenite remained small, below 1% according to the EBSD data. The austenite islands were preferentially located in areas where the martensite blocks were extremely fine.

Fig. 8 presents a bright-field TEM image of the sample aged for 3 h at 500 °C. At this relatively low magnification, individual martensitic laths were visible. In addition to the martensite, small spherical oxide particles were present throughout the microstructure. They appeared to be homogeneously distributed and were according to the APT data Al_2O_3 (not presented here).

3.5. Precipitate evaluation

3.5.1. Aging for 15 min

After 15 min aging, clustering of Ti and Nb can be discerned in the APT atom maps in Fig. 9. Isosurfaces, constructed based on Ni + Ti + Al + Nb (14at%), revealed a high number density of clusters, see Fig. 9b. The clusters had an average radius of about 0.5 nm. Based on the isosurfaces, the composition, Table 5, and number density of the clusters were calculated, see Table 6. In addition to the clusters, a thin region free of precipitates/cluster was observed, believed to be a thin film (about 20 nm wide) of austenite.

3.5.2. Aging for 3 h

After 3 h, precipitation of Ni, Nb, Ti, Al, Mn and to some extent Si, can be seen from the atom maps in Fig. 10a. Similar to the 15 min aged sample, an austenite film was present in the analysis, see Fig. 10b. The precipitates seemed to have a slow growth rate, as the average precipitate radius after 3 h was only around 1.4 nm. The number density of precipitates decreased slightly relative to the 15 min condition; however, the total volume fraction was found to increase (see Table 6). Furthermore, precipitates enriched in Nb together with Ti and Ni were found to form preferentially on

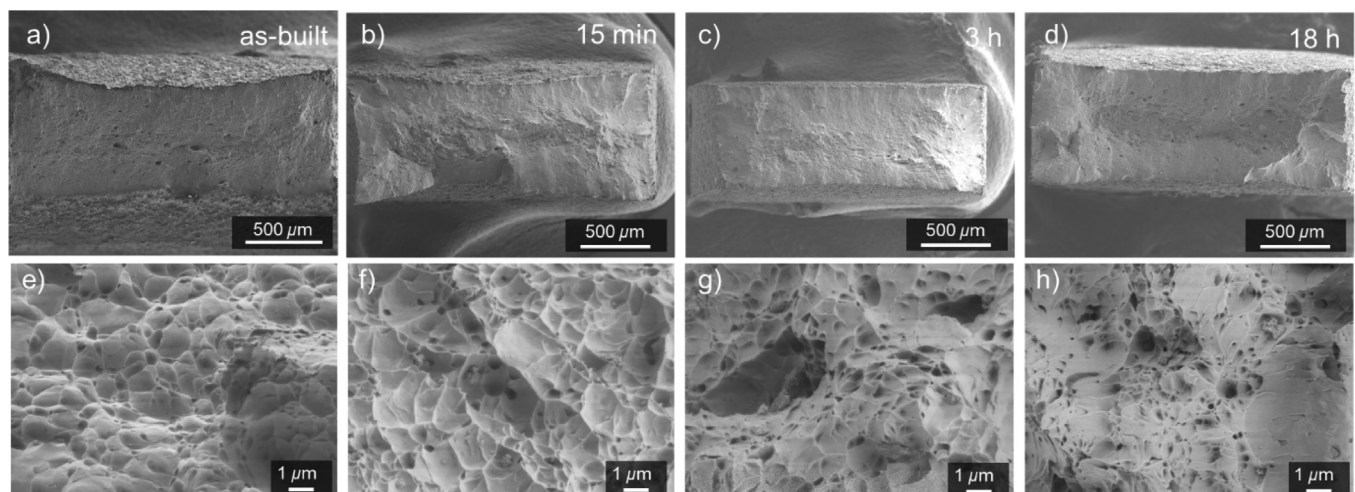


Fig. 3. Fracture surfaces of tensile specimens in the as-built state (a, e), aged for 15 min (b, f), aged for 3 h (c, g), and aged for 18 h (d, h). Overview in a-d and higher magnification images in e-h.

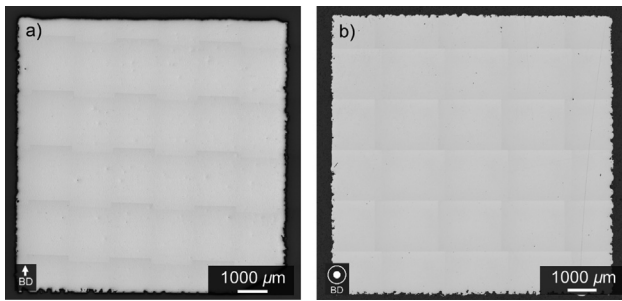


Fig. 4. Polished cross section of an as-built cube that was sectioned a) parallel and b) perpendicular to the building direction.

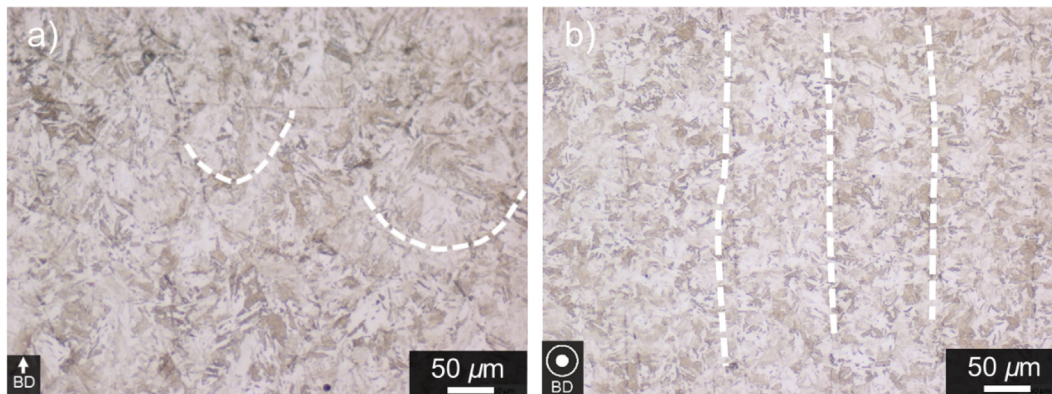


Fig. 5. Etched cross-sections a) parallel and b) perpendicular to the building direction. Some melt-pool borders are highlighted.

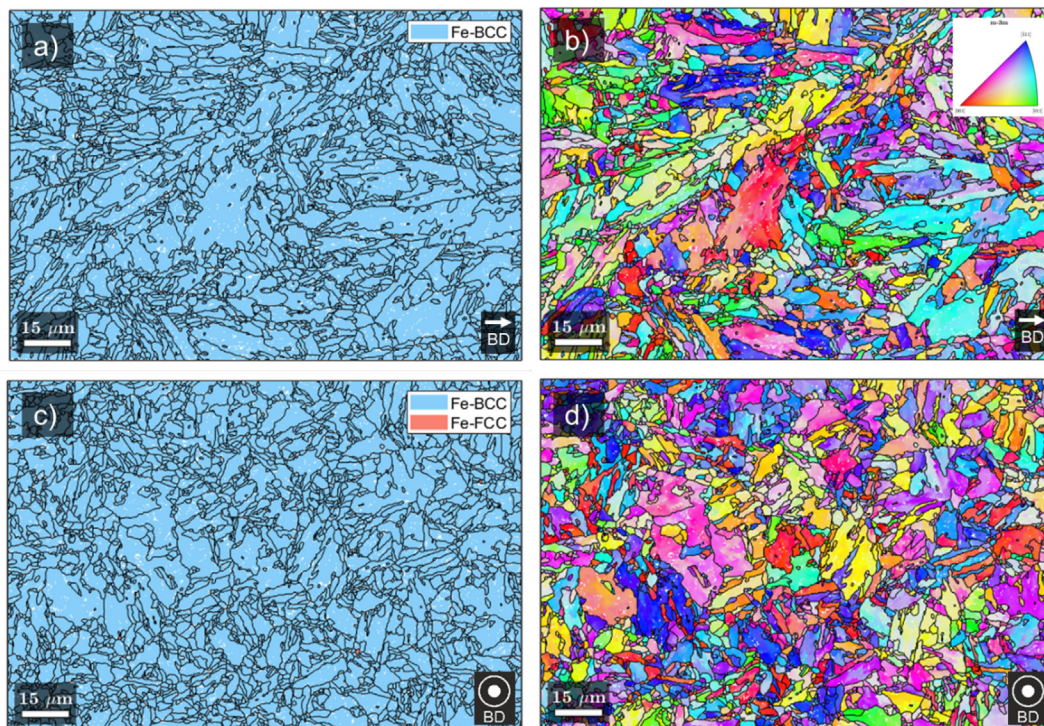


Fig. 6. EBSD phase (a, c) and orientation (z) maps (b, d) of the as-built state parallel (a, b) and perpendicular (c, d) to the building direction. The blue phase is martensite (Fe-BCC) and the salmon-colored phase is austenite (Fe-FCC). (For interpretation of the references to color in this figure legend, the reader is referred to the web version of this article.)

dislocations, see Fig. 10c (this could be seen clearer when the APT-map was rotated). Similar to the 15 min aged condition, the precipitates seemed to be compositionally of one family. However, an analysis of the radial distribution functions revealed that the elements tend to have clustering preferences. Nb and Al were co-clustering to a lower degree than Nb-Nb and Al-Al, but also compared to Nb-Ti and Al-Ti. Additionally, Si clustered with Nb and less with Al, and Mn was more clustered with Al and less with Nb. The average composition of the precipitates at this stage is presented in Table 7.

The microstructure was further analyzed using TEM with micrographs presented in Fig. 11. Higher magnification micrographs showed diffuse circular features, shown with arrows in Fig. 11b, with a radius between 1 and 2 nm. It is highly probable

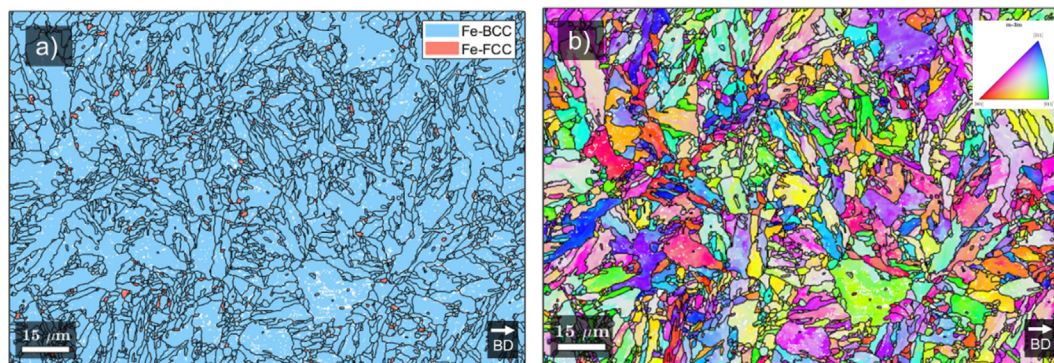


Fig. 7. EBSD phase (a) and orientation (z) maps (b) after aging at 500 °C for 3 h. The blue phase is martensite (Fe-BCC) and the salmon colored phase is austenite (Fe-FCC). (For interpretation of the references to color in this figure legend, the reader is referred to the web version of this article.)

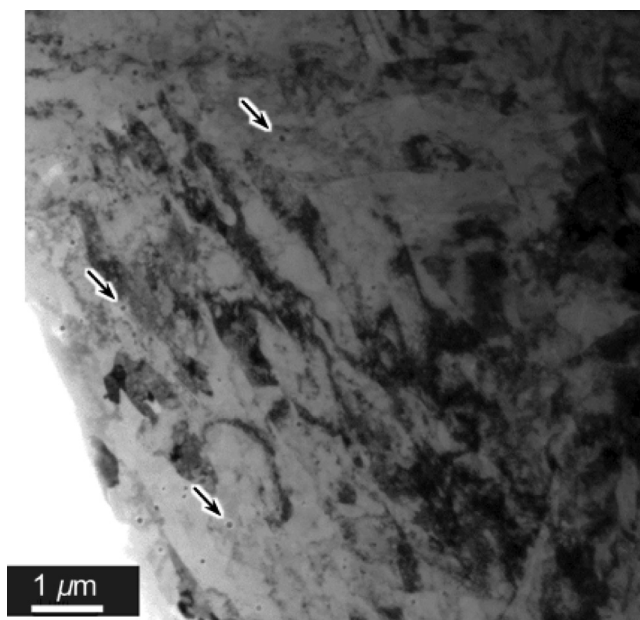


Fig. 8. Bright-field TEM micrograph of sample aged for 3 h at 500 °C, arrows indicate the location of oxide particles (<50 nm in size).

that these were precipitates, as the size and morphology were similar to the APT analysis. However, selective area diffraction did not reveal additional reflections to those of martensite.

3.5.3. Aging for 18 h

After 18 h of aging the precipitates had undergone a splitting phenomenon where several unique precipitate families formed. As the precipitates were often in direct contact with each other, precipitate splitting was the most probable mechanism of formation as opposed to co-nucleation. Fig. 12a shows some of the splitting where Nb and Al formed unique precipitates (see Nb and Al atom maps). Also, Mn and Si were segregating to different precipitate types. Fig. 12c shows an elemental profile through one of the split precipitates, highlighting the strong splitting of Al and Nb. One of the split variants had grown into large (radius >10 nm) precipitates rich in Ni, Al, Ti and Nb while being depleted of Fe, Cr, Si and Mn, believed to be η -phase. Another precipitate variant that had rapidly grown was rich in Ni, Si, Nb and Ti with low levels of Al and Mn. Examples of this precipitate can be seen in the right and left top corners of the atom maps in Fig. 12, believed to be G-phase. Finally, despite some precipitates splitting and growing into clearly differentiated compositions, i.e., η or G-phase, many precipitates remain small and compositionally complex. Further analysis of these precipitates reveals that they can be separated into two composition families. One where the precipitates are enriched in Nb, Ti and Si while the other is enriched in Al and Mn – suggesting that they are possibly transforming into G-phase and B2-NiAl, respectively. All of the split precipitate variants are still Ni-rich.

The compositions of the split variants together with assumed phases are presented in Table 8. The phase assumed to be γ' , or $L1_2$ -Ni₃X, was divided further into an Al-rich type with a relatively high Mn content (γ'_1), and a Nb, Si-rich precipitate with a composition resembling G-phase (γ'_2). The high Al content of γ'_1 in com-

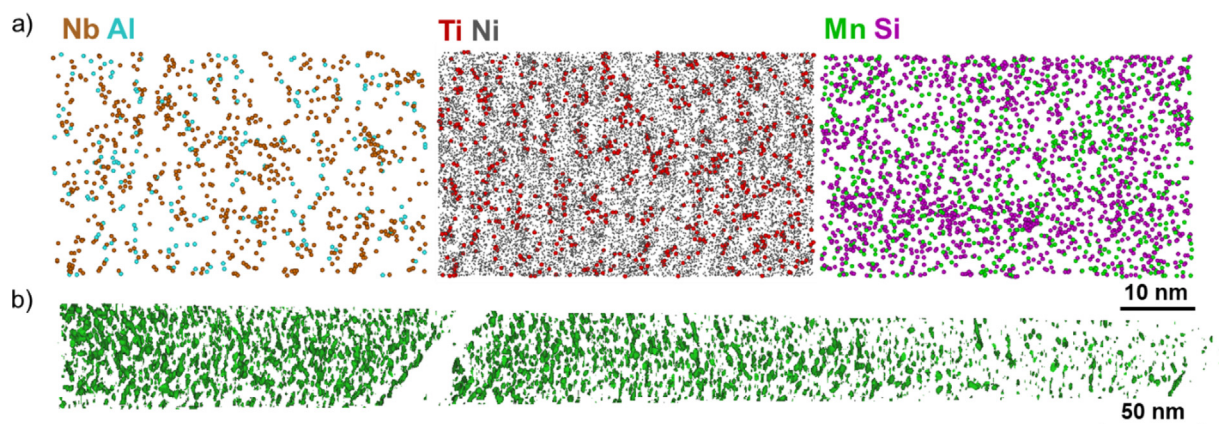


Fig. 9. a) Atom maps from a 5 nm slice after 15 min of aging. b) Isosurfaces of Ni + Ti + Al + Nb (14at%). The Ni atoms are drawn smaller than the other for clarity.

Table 5

Average chemical composition of the clusters after 15 min of aging (at%), calculated from the isosurfaces. Fe and Cr were excluded.

Ni	Al	Nb	Ti	Mn	Si
62.1	20.2	5.3	5.1	1.8	5.4

Table 6

Measured (APT) and calculated precipitate data. For 15 min the maximum separation method was used, whereas isosurfaces were used for 3 and 18 h.

Aging Time	Number Density (m^{-3})		Average Radius (nm)		Volume Fraction (%)	
	Measured	Simulated (Prisma)	Measured	Simulated (Prisma)	Measured	Simulated (Prisma)
15 min	1.5×10^{24}	7×10^{22}	0.5	0.3	0.10	0.0006
3 h	1.3×10^{24}	1.0×10^{24}	1.4	1.1	2.3	0.5
18 h	0.8×10^{24}	1.0×10^{24}	2.0	2.0	5.2	3.2
90 h	–	0.7×10^{24}	–	2.5	–	4.6

bination with the lower Ni content suggests that it could be B2-NiAl.

After 18 h the precipitates became more visible in TEM, as seen in Fig. 13b. However, the selected area diffraction pattern did not show any additional reflections to those of martensite. Fig. 14

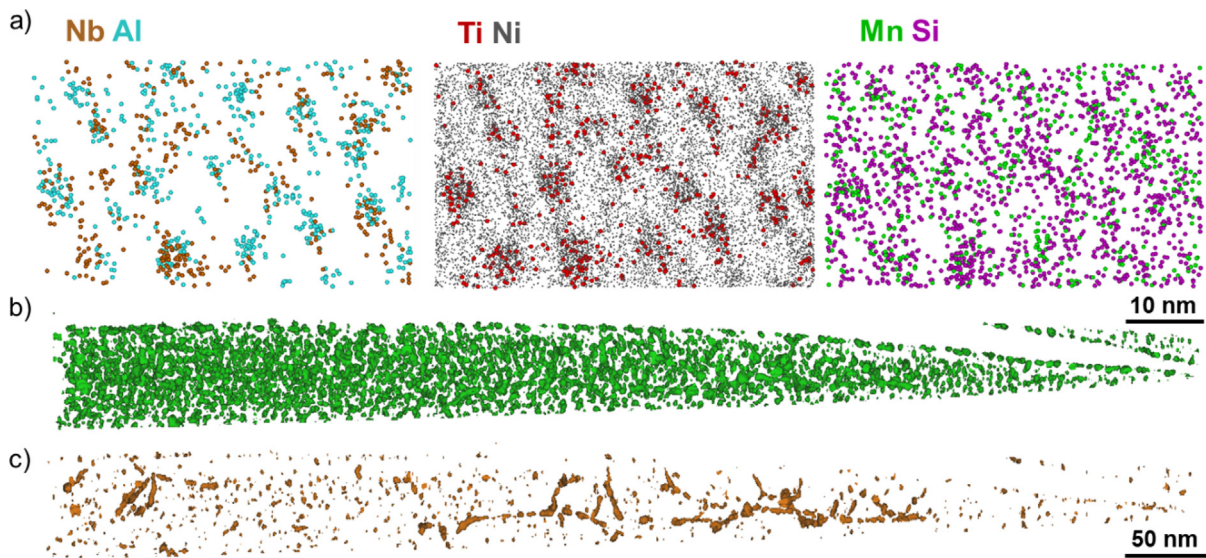


Fig. 10. a) Atom maps from a 5 nm slice after 3 h of aging. b) Isosurfaces of Ni + Ti + Al + Nb (18at%). c) Isosurfaces of Nb (1.5at%), showing precipitation along dislocations. The Ni atoms are drawn smaller than the other for clarity.

Table 7

Average chemical composition of the precipitates after 3 h of aging (at%), calculated from the isosurfaces. Fe and Cr were excluded.

Ni	Al	Nb	Ti	Mn	Si
61.2	23.6	4.0	4.3	2.1	4.7

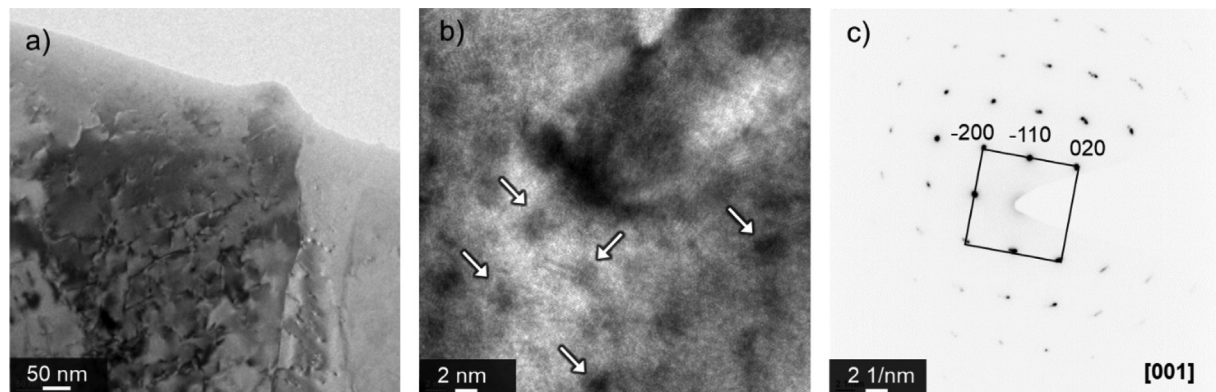


Fig. 11. Bright-field TEM micrographs (a, b), with arrows highlighting the precipitates. A selected area diffraction pattern (c) of sample aged for 3 h at 500 °C.

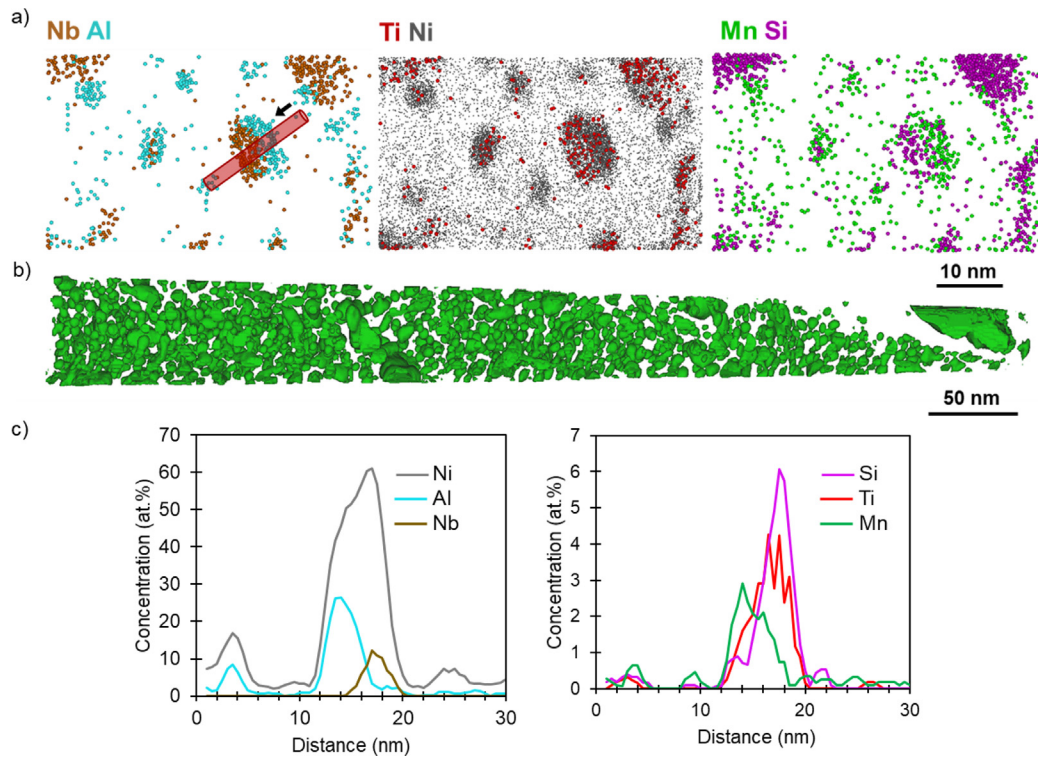


Fig. 12. a) Atom maps from a 5 nm slice after 18 h of aging. b) Isosurfaces of Ni + Ti + Al + Nb (22at%). c) 1D elemental profile of one of the split precipitates, diameter of the cylinder was 5 nm.

Table 8

Composition of individual precipitates measured with APT (at%) in the material aged for 18 h. The precipitates were defined by isosurfaces. Peak decomposition was used, Fe and Cr were excluded.

Assumed phase	Ni	Al	Nb	Ti	Mn	Si
G	57.9	1.8	12.4	7.1	0.3	20.5
η	72.2	17.9	4.6	4.2	0.2	0.7
γ'_1^*	55.5	32.7	1.3	2.4	6.0	2.0
γ'_2^*	59.9	6.4	12.8	7.5	1.0	12.3

* The assumed γ' -phase is divided into two different variants.

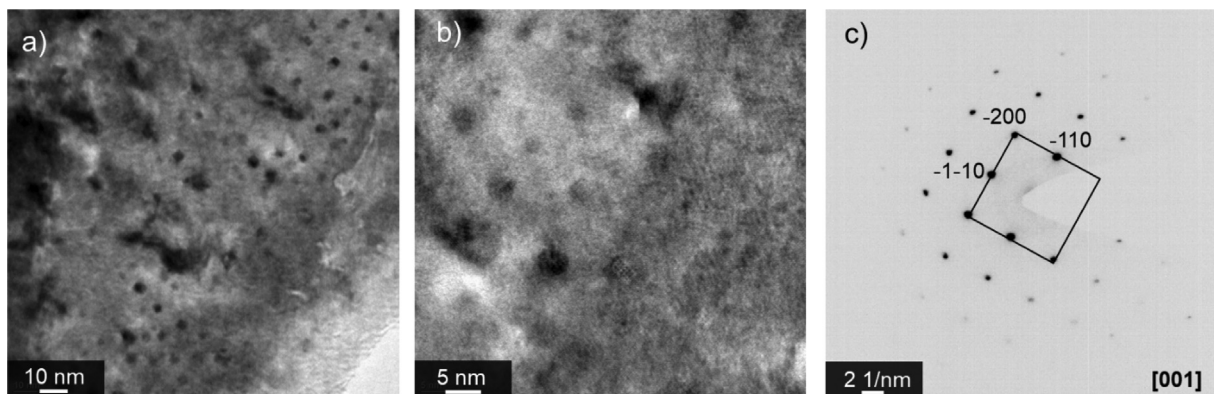


Fig. 13. Bright-field TEM micrographs (a,b) and a selected area diffraction (c) of sample aged for 18 h at 500 °C.

shows a high-resolution TEM image of a precipitate together with a fast-Fourier transform (FFT). The FFT revealed additional reflections, which were identified to originate from G-phase. The following orientational relationship was found: $(440)_G // (110)_M$, $(080)_G // (020)_M$ and $[001]_G // [001]_M$. Meaning that there is a cube-on-cube orientational relationship.

3.6. Matrix

The matrix composition was measured by APT throughout the different aging times and is presented in Table 9. After 18 h many of the precipitate forming elements are close to depletion, especially Nb and Ti. Hence, these elements cannot form new precipi-

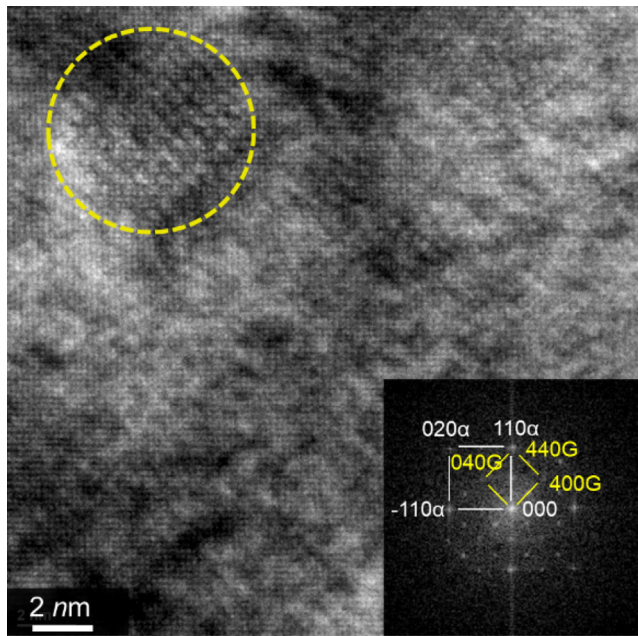


Fig. 14. High-resolution TEM image of a precipitate with an inset of an FFT that shows additional reflections to those of martensite, identified to originate from G-phase.

tates by prolonged aging, while Al, Mn and Si can still theoretically form new precipitates. Additionally, Ni is also being co-depleted as it is a constituent in all precipitates.

3.7. Results of precipitation simulations

As a tool for better understanding the precipitate evolution in the material, a simulation of precipitation at 500 °C was performed using the PRISMA module in the Thermo-Calc software package. The precipitation of L1₂-Ni₃X was simulated to test the validity of the designed microstructure, as predicted by the equilibrium calculation, see Table 2.

The general model in the PRISMA module was used. The experimental results from the APT study as summarized in Table 6 were used to calibrate the calculations. Any two of the three quantities; number density, average precipitate radius, and volume fraction, can be used for the calibration. In this work the number density and the average radius were used for practical reasons. Bulk nucleation was selected, and the number of nucleation sites was adjusted in a manual procedure to obtain the measured number density of precipitates in the calculations. To calibrate the calculated precipitate size to the measured size of the precipitates, a mobility enhancement factor of 4 was introduced. The agreement of calculations with measurements is then acceptable. This enhancement factor can be motivated by the highly dislocated martensitic microstructure in the as-printed material in which diffusion is accelerated. The interfacial energy was also adjusted to the measured mean radius, by a manual procedure. The finally selected simulation parameters are shown in Table 10.

Table 9
Matrix composition at various aging times, given in at%. Fe is balance.

	Cr	Ni	Al	Mo	Nb	Ti	Mn	Si
15 min	14.3	5.7	1.15	0.32	0.21	0.22	0.21	0.84
3 h	14.6	5.1	0.65	0.38	0.11	0.09	0.18	0.53
18 h	14.9	3.8	0.36	0.34	0.04	0.04	0.14	0.20

The simulations show results that are in line with the observations by APT, see Table 6. The main features of a high nucleation rate, a high number density of precipitates, and very good temperature resistance, with low coarsening rates are captured by the PRISMA simulations. The volume fraction increases slower than indicated by measurements.

The matrix composition at equilibrium with the FCC L1₂ phase at 500 °C is listed in Table 11. The solubility of Nb and Ti in the matrix is very low and in agreement with the measurements (Table 9), however, the calculated Al-content is higher than the measured matrix composition in Table 9. This can be the reason for the deviation between the measured and calculated volume fractions and originates from the thermodynamic description of the L1₂ phase.

In spite the deviation of the Al content in the matrix, it is clear that the thermodynamic description predicted an alloy composition that enables very stable precipitates. Fig. 15 shows how the amount of Al, Nb and Ti in the matrix affects the driving force for precipitation of the FCC L1₂ phase. High Nb contents give a large driving force, however high Nb contents can cause precipitation of unwanted phases. Ti increases the driving force up to a maximum at 0.3wt%. Increasing the Al content has a less pronounced effect on the driving force.

4. Discussion

This study had as a goal to develop a new stainless maraging steel variant for AM, more specifically LB-PBF. To accomplish this, many composition sets were screened using the CALPHAD methodology to reach a composition that is balanced with regard to corrosion resistance, precipitated phases and amount of retained austenite. The results confirm that the alloy design methodology successfully predicted printability of the alloy as well as its microstructure. The obtained microstructure was fully martensitic and directly hardenable, resulting in a rapid precipitation process with a high number density of precipitates. These properties led to mechanical properties that closely matched other stainless maraging grades.

The printing trials showed excellent printability requiring limited process optimization, meaning further process optimization is possible for increased process robustness. When printing using EOS parameters developed for 18Ni-300, the resulting residual porosity was below 0.05% and no cracks or other defects were detected. Indicating that this composition is robust to non-optimal printing parameters and in extension possesses good processability. As laser-based AM processes induce an intrinsic heat-treatment, early precipitation can be detrimental to the ductility of the matrix and can require additional heat-treatments prior to the aging heat treatment to bring the precipitated elements back in solution. However, the mechanical testing and microstructure evaluation showed that the formation of strengthening phases and detrimental phases (including austenite) were suppressed or held at sufficiently low levels during the printing. Thus, the calculations showing that precipitation of secondary phases would be suppressed during the LB-PBF process were found to be valid.

When aged, the material demonstrated rapid precipitation with a high number density of clusters forming already after 15 min.

Table 10
Parameters for the PRISMA simulation.

Nucleation Sites (m^{-3})	Interfacial Energy (J/m^2)	Mobility Enhancement Factor
1×10^{25}	0.12	4

Again, neither detrimental phases nor excessive amounts of austenite had formed during the aging process, confirming the validity of the simulations. Such cluster formation during the early stages of aging has previously been reported by Niu et al. [30] and Schober et al. [32] where the precipitate forming elements form coherent clusters that are homogeneously distributed within the matrix. Comparing the early precipitation rate to the works of Schober et al. [32] and Thuvander et al. [33], where conventionally manufactured stainless maraging variants were investigated, shows similar precipitate sizes and number densities as found in this study. Therefore, it seems as if the LB-PBF processing does not introduce additional nucleation and diffusional paths to those that already exist within the highly dislocated martensitic structure [51,52]. When comparing to 18Ni-300, both conventionally processed and laser metal deposited, the number density was nearly a magnitude higher in the composition investigated here [19]. Hence, the design goal of having similar or greater precipitate densities to 18Ni-300 was fulfilled. Despite the small size of the clusters, the mechanical properties significantly increased relative to the as-built state, from 815 MPa to 1408 MPa in yield strength with nearly negligible loss in ductility.

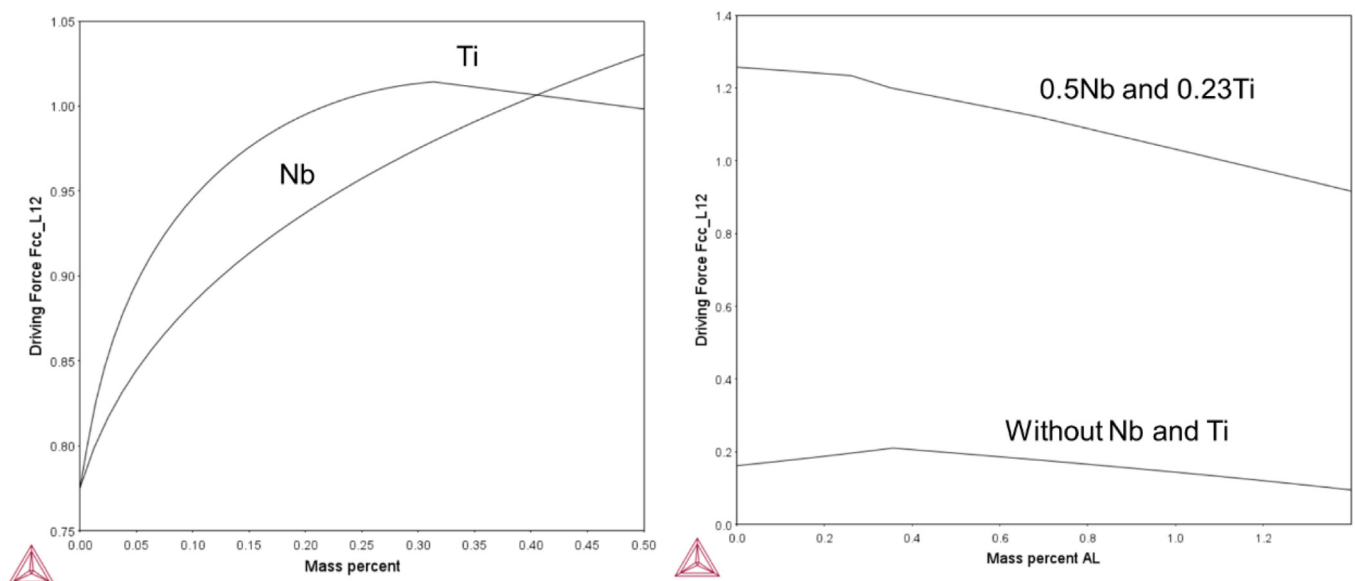
Further aging, total duration of 3 h, led to the formation of distinct precipitates that compositionally were very similar to the previously mentioned clusters. The precipitate composition fits well with the simulated $\text{L}_{12}\text{-Ni}_3\text{X}$ precipitate. Crystallographic

determination by TEM proved difficult due to the small size and relatively small volume fraction of these precipitates. Typically, steels of similar compositions are strengthened either by $\eta\text{-Ni}_3\text{Ti}$ [18,30,32] or B2-NiAl [22,32,53], yet this material exhibits precipitates that resemble a type of $\gamma'\text{-Ni}_3\text{X}$ precipitate that has previously been reported in the material Nanoflex [26]. The presence of $\gamma'\text{-Ni}_3\text{X}$ can be supported by the following findings: the relatively high (1:2) Ni to Al, Ti, Nb, Si ratio, the high Si-content, and finally it was predicted in the Thermo-Calc simulations in the form of $\text{L}_{12}\text{-Ni}_3\text{X}$. For η -phase to form, Si has to first be rejected from the pre-cursor precipitate [26,32]. For these reasons it seems unlikely that η -phase is forming at 3 h. This was also shown at longer aging times by APT, where there is a division between larger and smaller $\text{L}_{12}\text{-Ni}_3\text{X}$ precipitates where the larger were devoid of Si as opposed to the smaller - indicating that η -phase forms from $\gamma'\text{-Ni}_3\text{X}$.

The splitting of Al and Nb in the precipitates after 18 h resulted in at least three different types of precipitates according to the APT analysis. Through high-resolution TEM it was possible to identify that one of these is G-phase, with a cube-on-cube orientational relationship that previously has been reported in a ferritic stainless steel [54,55]. The formation of G-phase probably occurs after the initial splitting, where Al is rejected from the precipitates, hence allowing for Si to diffuse into the precipitate and form G-phase. Another precipitate type is believed to be $\eta\text{-Ni}_3\text{Ti}$ due to its low concentration of both Mn and Si, as mentioned earlier. Finally, the γ' found after 3 h of aging is de-composing into two separate precipitate types, one that appears to be a pre-cursor to G-phase (γ'_2) and one that is rich in Al with enrichments in Mn and Si (γ'_1). The latter is hypothesized to still be γ' , however, it may also be B2-NiAl due to the high Al content and the decreasing Ni-content. $\eta\text{-Ni}_3\text{Ti}$ and γ' (or B2-NiAl) were, however, not confirmed

Table 11
Calculated composition of the matrix in equilibrium with $\text{L}_{12}\text{-Ni}_3\text{X}$ precipitates at 500 °C.

	Cr	Ni	Al	Si	Mn	Mo	Nb	Ti
at%	12	4.8	1.6	1.0	0.2	0.05	0	0

**Fig. 15.** Driving force for the precipitation of FCC L_{12} as a function of the a) Ti and Nb content and b) Al content.

by either high-resolution TEM or selected area diffraction. In addition, the Nb-rich precipitates that were preferentially situated at dislocations might be a unique precipitate.

Similar precipitate splitting has been reported [32,56] where a pre-cursor phase separates into more thermodynamically favored variants. Significant elemental partitioning was reported throughout the splitting process to accommodate the solubility limits of each precipitate type. This splitting phenomenon is most probably responsible for the sluggish coarsening response within this material, where transformation to more thermodynamically stable variants is favored as opposed to classical coarsening. It is also likely that the precipitates will continue transforming until thermodynamic equilibrium is reached. Yet, based on the matrix composition, it is also possible that the precipitates have now reached the coarsening stage – as most of the precipitate forming elements are now depleted. From a mechanical performance perspective, despite reaching peak hardness the division resulted in a significant decrease in ductility, hence, shorter aging times are preferred for balanced static properties.

The alloy studied in the present work was designed to obtain a high fraction and density of L1₂-Ni₃X type precipitates to achieve a good hardening response. The experimental work shows that this was successful for the designed composition, and a high density of extremely small precipitates were formed after short heat treatment times. The rapid and dense precipitation can be understood to be a result of the high stability of the precipitates, which also gives a slow growth and coarsening. For a further optimization of properties, a lower total fraction of precipitates, and larger sizes could possibly have advantages. However, the effect of the microstructural evolution in LB-PBF materials on the precipitation can be difficult to predict. Based on the results of this study in comparison with earlier studies of stainless maraging variants [32,33], it seems as if there is a minor influence of the LB-PBF induced microstructure. Although identical compositions were not compared. Therefore, it is possible that the novel microstructure created from LB-PBF processing affects precipitation kinetics, but its extent needs to be researched further.

The as-calculated composition of the precipitates (Table 2) is in good agreement with the measured composition of the precipitates after 3 h aging (Table 7), which supports the validity of the designed matrix composition. The amount of retained austenite is difficult to quantify since it is only present in very thin layers as visualized by APT. The APT measurements of the matrix composition confirm a high Cr content, as aimed for. The PRISMA calculation was used to simulate precipitation, and the experimental data was used for calibration. It was possible to fairly well reproduce the very rapid and dense precipitation process, with a good fit of the size evolution. This supports the phase identifications, although there is not an exact fit of the compositions. As this type of detailed information on precipitate and matrix compositions in this type of steel is scarce, it is not surprising that the thermodynamic databases do not provide the exact information. Higher order information on phase compositions, like those obtained in the present work, could be implemented in the databases for future versions, however, that was outside the scope of this study.

5. Conclusions

In this work, a Co-free stainless maraging steel with excellent printability by LB-PBF was designed using a computational alloy design strategy based on the CALPHAD methodology. Its printability, microstructure, aging response at 500 °C together with the mechanical properties were evaluated by dedicated microstructural analysis and APT. The results showed that the application of a CALPHAD approach to alloy design was successful. The main find-

ings to why the designed alloy composition was proven a success are concluded below:

- The designed alloyed composition showed good printability despite using non-optimized parameters, reaching densities of >99.5% with no defects.
- The as-printed state shows good ductility of 14%, making it robust for LB-PBF processing.
- In the as-printed state, the material has a martensitic matrix with negligible amount of austenite and no deleterious secondary phases.
- The precipitation process is suggested to be: (Ni, Al, Nb, Ti, Mn, Si) clusters (15 min) → γ' -Ni₃(Al, Ti, Nb, Si, Mn) (3 h) → γ' -Ni₃(Al, Ti, Nb, Si, Mn) + G-Ni₁₆Si₇(Ti, Nb)₆ + η -Ni₃(Al, Ti, Nb) (18 h). Alternatively, at 18 h the γ' decomposes into two Ni-rich precipitate types, one that appears to be a pre-cursor to G-phase and one that resembles B2-NiAl.
- The coarsening rate was found to be very low, with the precipitates reaching an average radius of only 2 nm after 18 h with the splitting phenomenon believed to be the reason behind this.
- The mechanical response associated with the splitting observed after 18 h resulted in negligible increase in tensile strength, 1590 MPa compared with 1560 MPa, but at the cost of a significant decrease in ductility.

6. Data availability

The raw/processed data required to reproduce these findings cannot be shared at this time as the data also forms part of an ongoing study.

Declaration of Competing Interest

The authors declare that they have no known competing financial interests or personal relationships that could have appeared to influence the work reported in this paper.

Acknowledgements

This work has been conducted in the framework of the Centre for Additive Manufacturing – Metal (CAM²), supported by the Swedish Governmental Agency of Innovation Systems (Vinnova). The APT and TEM investigations were performed at Chalmers Materials Analysis Laboratory (CMAL).

References

- [1] J. Inoue, S. Nambu, Y. Ishimoto, T. Koseki, Fracture elongation of brittle/ductile multilayered steel composites with a strong interface, *Scr. Mater.* 59 (10) (2008) 1055–1058, <https://doi.org/10.1016/j.scriptamat.2008.07.020>.
- [2] P. Bajaj, A. Hariharan, A. Kini, P. Kürsteiner, D. Raabe, E.A. Jägle, Steels in additive manufacturing: A review of their microstructure and properties, *Mater. Sci. Eng., A* 772 (2020) 138633, <https://doi.org/10.1016/j.msea.2019.138633>.
- [3] S. Kou, A criterion for cracking during solidification, *Acta Mater.* 88 (2015) 366–374, <https://doi.org/10.1016/j.actamat.2015.01.034>.
- [4] D.D. Gu, W. Meiners, K. Wissenbach, R. Poprawe, Laser additive manufacturing of metallic components: materials, processes and mechanisms, *Int. Mater. Rev.* 57 (3) (2012) 133–164, <https://doi.org/10.1179/1743280411Y.0000000014>.
- [5] D. Herzog, V. Seyda, E. Wycisk, C. Emmelmann, Additive manufacturing of metals, *Acta Mater.* 117 (2016) 371–392, <https://doi.org/10.1016/j.actamat.2016.07.019>.
- [6] W.J. Sames, F.A. List, S. Pannala, R.R. Dehoff, S.S. Babu, The metallurgy and processing science of metal additive manufacturing, *Int. Mater. Rev.* 61 (5) (2016) 315–360, <https://doi.org/10.1080/09506608.2015.1116649>.
- [7] P.A. Hooper, Melt pool temperature and cooling rates in laser powder bed fusion, *Addit. Manuf.* 22 (2018) 548–559, <https://doi.org/10.1016/j.addma.2018.05.032>.
- [8] C. Zhao, K. Fezzaa, R.W. Cunningham, H. Wen, F. Carlo, L. Chen, A.D. Rollett, T. Sun, Real-time monitoring of laser powder bed fusion process using high-

- speed X-ray imaging and diffraction, *Sci. Rep.* 7 (2017) 3602, <https://doi.org/10.1038/s41598-017-03761-2>.
- [9] U. Scipioni Bertoli, G. Guss, S. Wu, M.J. Matthews, J.M. Schoenung, In-situ characterization of laser-powder interaction and cooling rates through high-speed imaging of powder bed fusion additive manufacturing, *Mater. Des.* 135 (2017) 385–396, <https://doi.org/10.1016/j.matdes.2017.09.044>.
 - [10] G.M. Karthik, H.S. Kim, Heterogeneous Aspects of Additive Manufactured Metallic Parts: A Review, *Met. Mater. Int.* 27 (1) (2021) 1–39, <https://doi.org/10.1007/s12540-020-00931-2>.
 - [11] L. Leyssens, B. Vinck, C. Van der Straeten, F. Wuyts, L. Maes, Cobalt toxicity in humans—A review of the potential sources and systemic health effects, *Toxicology* 387 (2017) 43–56, <https://doi.org/10.1016/j.tox.2017.05.015>.
 - [12] World Health Organization, International Agency for Research on Cancer, IARC Working Group on the Evaluation of Carcinogenic Risks to Humans, eds., Cobalt in hard metals and cobalt sulfate, gallium arsenide, indium phosphide, and vanadium pentoxide, International Agency for Research on Cancer ; Distributed by WHO Press, Lyon, France : Geneva, Switzerland, 2006.
 - [13] T. Frankel, Apple cracks down further on cobalt supplier in Congo as child labor persists accessed December 7, 2021, *Washington Post* (2017). <https://www.washingtonpost.com/news/the-switch/wp/2017/03/03/apple-cracks-down-further-on-cobalt-supplier-in-congo-as-child-labor-persists/>.
 - [14] D. Reisinger, Apple Halts Cobalt Buy Over Supply Chain Child Labor Concerns accessed December 7, 2021, *Fortune* (2017). <https://fortune.com/2017/03/03/apple-cobalt-child-labor/>.
 - [15] J.-O. Andersson, T. Helander, L. Höglund, P. Shi, B. Sundman, Thermo-Calc & DICTRA, computational tools for materials science, *Calphad.* 26 (2002) 273–312, [https://doi.org/10.1016/S0364-5916\(02\)00037-8](https://doi.org/10.1016/S0364-5916(02)00037-8).
 - [16] S. Bodziak, K.S. Al-Rubaie, L.D. Valentina, F.H. Lafratta, E.C. Santos, A.M. Zanatta, Y. Chen, Precipitation in 300 grade maraging steel built by selective laser melting: Aging at 510 °C for 2 h, *Mater. Charact.* 151 (2019) 73–83, <https://doi.org/10.1016/j.matchar.2019.02.033>.
 - [17] C. Tan, K. Zhou, M. Kuang, W. Ma, T. Kuang, Microstructural characterization and properties of selective laser melted maraging steel with different build directions, *Sci. Technol. Adv. Mater.* 19 (1) (2018) 746–758, <https://doi.org/10.1080/14686996.2018.1527645>.
 - [18] E.A. Jägle, P.-P. Choi, J. Van Humbeeck, D. Raabe, Precipitation and austenite reversion behavior of a maraging steel produced by selective laser melting, *J. Mater. Res.* 29 (17) (2014) 2072–2079, <https://doi.org/10.1557/jmr.2014.204>.
 - [19] E.A. Jägle, Z. Sheng, P. Kürsteiner, S. Ocylok, A. Weisheit, D. Raabe, Comparison of Maraging Steel Micro- and Nanostructure Produced Conventionally and by Laser Additive Manufacturing, *Materials*. 10 (2017) 8, <https://doi.org/10.3390/ma10010008>.
 - [20] F.F. Conde, J.D. Escobar, J.P. Oliveira, M. Bérese, A.L. Jardini, W.W. Bose, J.A. Avila, Effect of thermal cycling and aging stages on the microstructure and bending strength of a selective laser melted 300-grade maraging steel, *Mater. Sci. Eng., A* 758 (2019) 192–201, <https://doi.org/10.1016/j.msea.2019.03.129>.
 - [21] F.F. Conde, J.A. Avila, J.P. Oliveira, N. Schell, M.F. Oliveira, J.D. Escobar, Effect of the as-built microstructure on the martensite to austenite transformation in a 18Ni maraging steel after laser-based powder bed fusion, *Addit. Manuf.* 46 (2021), <https://doi.org/10.1016/j.addma.2021.102122>.
 - [22] Z. Guo, W. Sha, D. Vaumousse, Microstructural evolution in a PH13-8 stainless steel after ageing, *Acta Mater.* 51 (1) (2003) 101–116, [https://doi.org/10.1016/S1359-6454\(02\)00353-1](https://doi.org/10.1016/S1359-6454(02)00353-1).
 - [23] D.H. Ping, M. Ohnuma, Y. Hirakawa, Y. Kadoya, K. Hono, Microstructural evolution in 13Cr–8Ni–2.5Mo–2Al martensitic precipitation-hardened stainless steel, *Mater. Sci. Eng., A* 394 (2005) 285–295, <https://doi.org/10.1016/j.msea.2004.12.002>.
 - [24] Z.H. Wang, B. Niu, Q. Wang, C. Dong, J.C. Jie, T.M. Wang, T.G. Nieh, Designing ultrastrong maraging stainless steels with improved uniform plastic strain via controlled precipitation of coherent nanoparticles, *J. Mater. Sci. Technol.* 93 (2021) 60–70, <https://doi.org/10.1016/j.jmst.2021.04.011>.
 - [25] R. Schnitzer, R. Radis, M. Nöhrer, M. Schober, R. Hochfellner, S. Zinner, E. Povoden-Karadeniz, E. Kozeschnik, H. Leitner, Reverted austenite in PH 13–8 Mo maraging steels, *Mater. Chem. Phys.* 122 (1) (2010) 138–145, <https://doi.org/10.1016/j.matchemphys.2010.02.058>.
 - [26] M. Thuvander, M. Andersson, K. Stiller, Precipitation process of martensitic PH stainless steel Nanoflex, *Mater. Sci. Technol.* 28 (6) (2012) 695–701, <https://doi.org/10.1179/1743284711Y.0000000115>.
 - [27] S. Ifergane, M. Pinkas, Z. Barkay, E. Brosh, V. Ezersky, O. Beerli, N. Eliaz, The relation between aging temperature, microstructure evolution and hardening of Custom 465® stainless steel, *Mater. Charact.* 127 (2017) 129–136, <https://doi.org/10.1016/j.matchar.2017.02.023>.
 - [28] V.K. Vasudevan, S.J. Kim, C.M. Wayman, Precipitation reactions and strengthening behavior in 18 Wt Pct nickel maraging steels, *Metall Mater Trans A*. 21 (10) (1990) 2655–2668, <https://doi.org/10.1007/BF02646061>.
 - [29] S.-J. Kim, C.M. Wayman, Precipitation behavior and microstructural changes in maraging Fe–Ni–Mn–Ti alloys, *Mater. Sci. Eng., A* 128 (1990) 217–230, [https://doi.org/10.1016/0921-5093\(90\)90230-Z](https://doi.org/10.1016/0921-5093(90)90230-Z).
 - [30] M. Niu, G. Zhou, W. Wang, M.B. Shahzad, Y. Shan, K. Yang, Precipitate evolution and strengthening behavior during aging process in a 2.5 GPa grade maraging steel, *Acta Mater.* 179 (2019) 296–307, <https://doi.org/10.1016/j.actamat.2019.08.042>.
 - [31] M.C. Niu, L.C. Yin, K. Yang, J.H. Luan, W. Wang, Z.B. Jiao, Synergistic alloying effects on nanoscale precipitation and mechanical properties of ultrahigh-strength steels strengthened by Ni3Ti, Mo-enriched, and Cr-rich co-precipitates, *Acta Materialia*. 209 (2021), <https://doi.org/10.1016/j.actamat.2021.116788>.
 - [32] M. Schober, R. Schnitzer, H. Leitner, Precipitation evolution in a Ti-free and Ti-containing stainless maraging steel, *Ultramicroscopy* 109 (5) (2009) 553–562, <https://doi.org/10.1016/j.ultramic.2008.10.016>.
 - [33] M. Thuvander, M. Andersson, K. Stiller, Multiple Influences of Molybdenum on the Precipitation Process in a Martensitic PH Stainless Steel, *Metals*. 9 (2019) 1118, <https://doi.org/10.3390/met9101118>.
 - [34] P. Liu, A.H. Stigenberg, J.-O. Nilsson, Isothermally formed quasicrystalline precipitates used for strengthening in a new maraging stainless steel, *Scr. Metall. Mater.* 31 (3) (1994) 249–254, [https://doi.org/10.1016/0956-716X\(94\)90278-X](https://doi.org/10.1016/0956-716X(94)90278-X).
 - [35] D. Dong, C. Chang, H. Wang, X. Yan, W. Ma, M. Liu, S. Deng, J. Gardan, R. Bolot, H. Liao, Selective laser melting (SLM) of CX stainless steel: Theoretical calculation, process optimization and strengthening mechanism, *J. Mater. Sci. Technol.* 73 (2021) 151–164, <https://doi.org/10.1016/j.jmst.2020.09.031>.
 - [36] X. Yan, C. Chen, C. Chang, D. Dong, R. Zhao, R. Jenkins, J. Wang, Z. Ren, M. Liu, H. Liao, R. Lupoi, S. Yin, Study of the microstructure and mechanical performance of C-X stainless steel processed by selective laser melting (SLM), *Mater. Sci. Eng., A* 781 (2020), <https://doi.org/10.1016/j.msea.2020.139227>.
 - [37] J. Samei, H. Asgari, C. Pelligra, M. Sanjari, S. Salavati, A. Shahriari, M. Amiraleki, M. Jahanbakht, A. Hadadzadeh, B.S. Amirkhiz, M. Mohammadi, A hybrid additively manufactured martensitic-maraging stainless steel with superior strength and corrosion resistance for plastic injection molding dies, *Addit. Manuf.* 45 (2021), <https://doi.org/10.1016/j.addma.2021.102068>.
 - [38] A. Hadadzadeh, A. Shahriari, B.S. Amirkhiz, J. Li, M. Mohammadi, Additive manufacturing of an Fe–Cr–Ni–Al maraging stainless steel: Microstructure evolution, heat treatment, and strengthening mechanisms, *Mater. Sci. Eng., A* 787 (2020), <https://doi.org/10.1016/j.msea.2020.139470>.
 - [39] P. Krakhmalev, G. Fredriksson, M. Thuvander, M. Åsberg, A.M. Vilarde, C. Oikonomou, G. Maistro, A. Medvedeva, N. Kazantseva, Influence of heat treatment under hot isostatic pressing (HIP) on microstructure of intermetallic-reinforced tool steel manufactured by laser powder bed fusion, *Mater. Sci. Eng., A* 772 (2020), <https://doi.org/10.1016/j.msea.2019.138699>.
 - [40] T. Gladman, Precipitation hardening in metals, *Mater. Sci. Technol.* 15 (1) (1999) 30–36, <https://doi.org/10.1179/026708399773002782>.
 - [41] E. Orowan, Symposium on internal stresses in metals and alloys, *Institute of Metals, London*. 451 (1948).
 - [42] M. Ashby, Oxide dispersion strengthening, in: *AIME Conf. Proc.*, New York, 1958: p. 143.
 - [43] E. Nembach, Precipitation hardening caused by a difference in shear modulus between particle and matrix, *Phys. Stat. Sol. (a)* 78 (2) (1983) 571–581.
 - [44] R. Schnitzer, S. Zinner, H. Leitner, Modeling of the yield strength of a stainless maraging steel, *Scr. Mater.* 62 (5) (2010) 286–289, <https://doi.org/10.1016/j.scriptamat.2009.11.020>.
 - [45] S. Sun, M. Brandt, M. Easton, Powder bed fusion processes: An overview, *Laser Additive Manuf.* (2017) 55–77.
 - [46] F. Bachmann, R. Hielscher, H. Schaeben, Texture analysis with MTEX – free and open source software toolbox, *Solid State Phenom.* 160 (2010) 63–68, <https://doi.org/10.4028/www.scientific.net/SSP.160.63>.
 - [47] M.K. Miller, R.G. Forbes, The Local Electrode Atom Probe, in: M.K. Miller, R.G. Forbes (Eds.), *Atom-Probe Tomography: The Local Electrode Atom Probe*, Springer US, Boston, MA, 2014: pp. 229–258. https://doi.org/10.1007/978-1-4899-7430-3_5.
 - [48] D. Vaumousse, A. Cerezo, P.J. Warren, A procedure for quantification of precipitate microstructures from three-dimensional atom probe data, *Ultramicroscopy* 95 (2003) 215–221, [https://doi.org/10.1016/S0304-3991\(02\)00319-4](https://doi.org/10.1016/S0304-3991(02)00319-4).
 - [49] A. Kolhatkar, V. Karthik, G.M.S.K. Chaitanya, A. Kumar, D. Ramchandran, Development and validation of a miniature tensile specimen for determination of mechanical properties, *JTE*. 47 (2019) 3417–3431, <https://doi.org/10.1520/JTE20180294>.
 - [50] G. Herbsleb, Influence of SO₂, H₂S and CO on Pitting Corrosion of Austenitic Chromium-Nickel Stainless Steels with up to 4 wt. % Molybdenum in 1 M NaCl, *Werkst. Korros.* 33 (1982) 334–340.
 - [51] E.I. Galindo-Nava, P.E.J. Rivera-Díaz-del-Castillo, Understanding the factors controlling the hardness in martensitic steels, *Scr. Mater.* 110 (2016) 96–100, <https://doi.org/10.1016/j.scriptamat.2015.08.010>.
 - [52] S. Morito, J. Nishikawa, T. Maki, Dislocation Density within Lath Martensite in Fe–C and Fe–Ni Alloys, *ISIJ Int.* 43 (9) (2003) 1475–1477, <https://doi.org/10.2355/isijinternational.43.1475>.
 - [53] Z.B. Jiao, J.H. Luan, Z.W. Zhang, M.K. Miller, C.T. Liu, High-strength steels hardened mainly by nanoscale NiAl precipitates, *Scr. Mater.* 87 (2014) 45–48, <https://doi.org/10.1016/j.scriptamat.2014.05.006>.
 - [54] M. Yang, Daniel J.M. King, I. Povstugar, Y. Wen, J. Luan, B. Kuhn, Z. Jiao, C. Wang, M.R. Wenman, X. Liu, Precipitation behavior in G-phase strengthened ferritic stainless steels, *Acta Materialia*. 205 (2021) 116542. <https://doi.org/10.1016/j.actamat.2020.116542>.
 - [55] A. Mateo, L. Llanes, M. Anglada, A. Redjaimia, G. Metauer, Characterization of the intermetallic G-phase in an AISI 329 duplex stainless steel, *J. Mater. Sci.* 32 (1997) 4533–4540, <https://doi.org/10.1023/A:1018669217124>.
 - [56] H. Leitner, M. Schober, R. Schnitzer, Splitting phenomenon in the precipitation evolution in an Fe–Ni–Al–Ti–Cr stainless steel, *Acta Mater.* 58 (4) (2010) 1261–1269, <https://doi.org/10.1016/j.actamat.2009.10.030>.